



# Lightning in superconductors

J. I. Vestgård<sup>1</sup>, D. V. Shantsev<sup>1</sup>, Y. M. Galperin<sup>1,2,4</sup> & T. H. Johansen<sup>1,3,4</sup>

## SUBJECT AREAS:

PHYSICS

CONDENSED-MATTER PHYSICS

STATISTICAL PHYSICS,  
THERMODYNAMICS AND  
NONLINEAR DYNAMICS

SUPERCONDUCTING PROPERTIES  
AND MATERIALS

Received  
6 June 2012

Accepted  
30 October 2012

Published  
26 November 2012

Correspondence and  
requests for materials  
should be addressed to  
J.I.V. (j.i.vestgard@  
fys.uio.no)

<sup>1</sup>Department of Physics, University of Oslo, P. O. Box 1048 Blindern, 0316 Oslo, Norway, <sup>2</sup>A. F. Ioffe Physico-Technical Institute RAS, 194021 St. Petersburg, Russian Federation, <sup>3</sup>Institute for Superconducting and Electronic Materials, University of Wollongong, Northfields Avenue, Wollongong, NSW 2522, Australia, <sup>4</sup>Centre for Advanced Study at the Norwegian Academy of Science and Letters, Drammensveien 78, 0271 Oslo, Norway.

**Crucially important for application of type-II superconductor films is the stability of the vortex matter – magnetic flux lines penetrating the material. If some vortices get detached from pinning centres, the energy dissipated by their motion will facilitate further depinning, and may trigger a massive electromagnetic breakdown. Up to now, the time-resolved behaviour of these ultra-fast events was essentially unknown. We report numerical simulation results revealing the detailed dynamics during breakdown as within nanoseconds it develops branching structures in the electromagnetic fields and temperature, with striking resemblance of atmospheric lightning. During a dendritic avalanche the superconductor is locally heated above its critical temperature, while electrical fields rise to several kV/m as the front propagates at instant speeds near up to 100 km/s. The numerical approach provides an efficient framework for understanding the ultra-fast coupled non-local dynamics of electromagnetic fields and dissipation in superconductor films.**

The smooth gradual penetration of magnetic flux in type-II superconductor films experiencing an increasing perpendicular magnetic field can be interrupted by large amounts of flux rushing in almost instantaneously. Left to be observed after such an event is the intriguing dendritic structure frozen in the flux distribution, see Ref. 1 for a review. This dramatic avalanche phenomenon has been observed in films of many materials, such as Nb<sup>2,3</sup>, YBa<sub>2</sub>Cu<sub>3</sub>O<sub>x</sub><sup>4–7</sup>, Pb<sup>8</sup>, MgB<sub>2</sub><sup>9–15</sup>, Nb<sub>3</sub>Sn<sup>16</sup>, YNi<sub>2</sub>B<sub>2</sub>C<sup>17</sup>, NbN<sup>18,19</sup>, and very recently also in  $\alpha$ -MoGe<sup>20</sup>. It is today widely accepted that such events originate from a thermoelectromagnetic instability<sup>21</sup>, where an initial fluctuation sets some flux in motion and the dissipative displacement increases the local temperature. This reduces the flux pinning, and facilitates even further motion of flux in the same region. Thus, a positive feedback loop is created, which may lead to a sudden catastrophic breakdown in the physical properties, and hence, also the potential practical use of the superconductor.

These events are extreme also because they occur unpredictably and develop too fast to be followed dynamically by any experimental method available today. With conventional magnetometry one observes only a step in the magnetic moment due to the abrupt redistribution of flux and induced currents<sup>22,23</sup>. More information is obtained from magneto-optical imaging (MOI), where the spatial distribution of magnetic flux before and after the breakdown is visualized using a Faraday-active sensor mounted on the sample<sup>24</sup>. However, results providing insight into how the breakdown evolves in time are extremely scarce. Only by using a femtosecond pulsed laser to actively trigger an event it was possible to synchronize the image recording and to capture the flux distribution at an intermediate stage<sup>5–7</sup>.

From those experiments it was found that the flux front advances in a nonballistic way with a velocity decaying in time. In the initial stage the front can advance at an astonishing speed of 100 km/s. This dramatic dynamics poses a long list of unresolved questions, in particular, (i) How do the electric field, temperature, and flow of shielding currents evolve during the breakdown? (ii) In a typical event many branches are formed. Do they grow simultaneously, or develop one by one from the same root? (iii) Where is the temperature maximum, at the tip or at the root of the dendritic structure, and does it exceed the critical temperature  $T_c$  of the superconductor? And (iv) Does there exist any physical activity that could serve as a warning that breakdown is near?

We have addressed these questions by performing numerical simulations of the thermo-electromagnetic behavior of a superconducting thin disk. The modelling is done using classical electromagnetism with a highly nonlinear material law<sup>25</sup> coupled to an equation describing the production and transfer of heat. In films, compared to bulk superconductors, the theoretical treatment is far more challenging due to the non-local electro-dynamics and the presence of a substrate at constant temperature  $T_0$  in close thermal contact with the sample<sup>26</sup>.

Linear stability analysis starting from a smooth critical-state flux distribution has provided the conditions for onset of the thermomagnetic instability. The most unstable mode has a finite wave-number, which means that the instability will nucleate by fingering<sup>27–31</sup>. As the instability develops, numerical analysis of the non-linear and

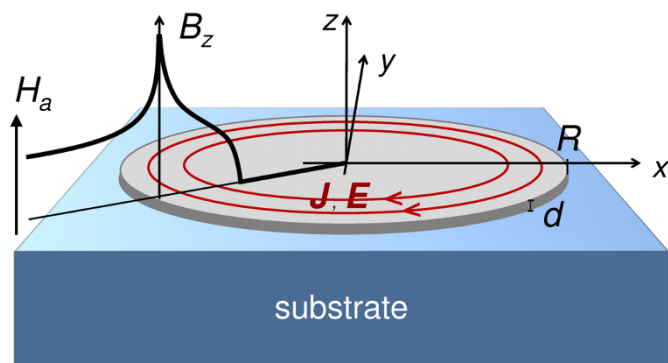


**Figure 1 | Sample configuration.** A thin superconducting disk on a substrate exposed to a gradually increasing perpendicular magnetic field,  $H_a$ . The flux density,  $B_z$ , is advancing from the edge along with a distribution of induced shielding current,  $J$ , and electrical field,  $E$ .

non-local dynamics of magnetic flux and temperature have revealed that the instabilities develop into complex branching structures<sup>28,32</sup>.

Here we focus on the temporal evolution of the instability – a complete scenario beyond experimental accessibility. Our results cover the nucleation stage of the breakdown, the branching stage when the dendritic pattern emerges, and finally the stagnation of flux motion and decay of the released heat. We explain the physical mechanisms involved at every stage of the event, and provide analytical expressions for all the relevant time scales.

## Results

**Flux penetration.** The simulations were carried out for a thin disk geometry (Fig. 1) using material parameters corresponding to superconducting  $\text{MgB}_2$ . The Methods section gives a description of the numerical approach. A magnetic field  $H_a$  is applied transverse to the sample plane, and as it gradually increases from zero it drives the penetration of magnetic flux into the disk. In the early stage of the field ramp, the flux enters evenly around the edge, and advances to increasing depth without any sign of intermittent behaviour. In the penetrated region a critical state is formed and characterized by a sheet current  $J$  and flux density  $B_z$  in full agreement with the Bean model for a thin circular disk<sup>33–35</sup>.

When the applied field reaches  $\mu_0 H_{\text{th}} = 5.3$  mT the first abrupt event is nucleated, and magnetic flux rushes in from the edge; see Supplementary Movie 1. A complex branching structure is created as the flux invades deep into the Meissner state region, which previously was free from flux, see Fig. 2a. As  $H_a$  continues increasing, only the gradual flux penetration resumes while the dendritic structure remains frozen. Then, at the field of 6.2 mT, another similar event takes place in a different part of the sample, and soon thereafter yet another one strikes. In this way the superconductor experiences a sequence of dramatic events at unpredictable intervals and locations, and where each breakdown follows an intriguing path in a macroscopically uniform medium. Since this phenomenon is of electrodynamic nature, it is interesting to recognize the many aspects that are similar to atmospheric lightning. One exception, however, is that in the superconductor the magnetic footprints are preserved, which has allowed experimental visualization of the phenomenon. Figure 2b shows an MOI picture of the flux distribution in a superconducting  $\text{MgB}_2$  film at  $T = 5$  K where the magnetic field had been increased from zero to  $\mu_0 H_a = 3.8$  mT. The experimental image reveals that the flux avalanches have a morphology quite similar to the numerical results, and also that the events have a clear tendency to avoid spatial overlap, as in the simulations.

Evidently, in a circular disk there is no geometrically preferred location for the first breakdown to nucleate. Instead, the place of the first event is selected by a combination of the quenched disorder

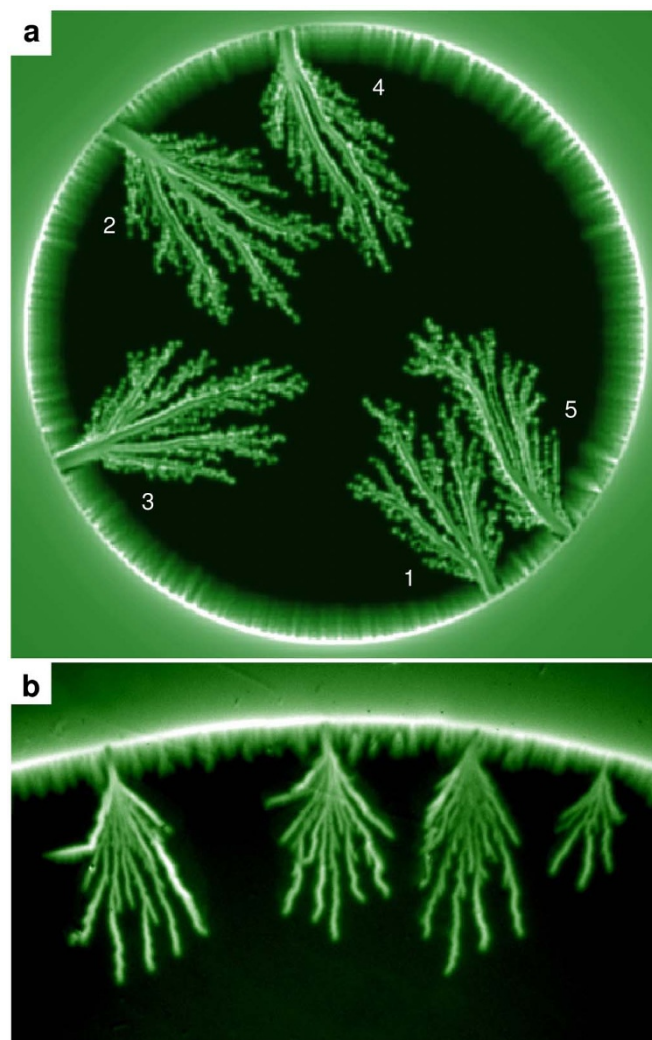


**Figure 2 | Flux density after a few breakdown events.** (a) Simulated distribution of  $B_z$  in a superconducting disk after five flux avalanches occurred in the sequence indicated by the numbers as the applied field was ramped up from zero to  $\mu_0 H_a = 8.5$  mT. (See Supplementary Movie 1.) (b) Magneto-optical image of the flux density in a superconducting  $\text{MgB}_2$  film cooled to 6 K and then exposed to an applied field of 3.8 mT.

and the random fluctuations. However, after the first event has occurred, the symmetry is broken because the flux avalanche destroys locally the critical-state, and thus reduces the shielding current near the edge where the flux enters. As a result, typical for films placed in a perpendicular magnetic field, the largest edge field is found in sectors between the roots of previous events. Hence, there is an anti-correlation in space and time between avalanches. The nucleation sites therefore tend to distribute evenly around the circumference, as one finds also experimentally (Fig. 2b).

Figure 3 shows the total magnetic flux  $\Phi = \int d^2r B_z(r)$  integrated over the disk area plotted as function of the increasing applied field. Initially, the  $\Phi(H_a)$  grows gradually until the threshold field of 5.3 mT is reached. Here  $\Phi$  makes a jump corresponding to entrance of 2.6 millions flux quanta, and forms the dendritic structure labelled (1) in the image. The subsequent jumps marked (2)–(5) involve a similar amount of flux. The flux entering during the intervals *between* subsequent jumps is also substantial, but smaller than the flux involved in each event.

**Electric field and temperature.** Far less accessible by experimental methods is the behaviour of the electric field  $E$  and temperature  $T$  in the superconductor, and we report here only results obtained from

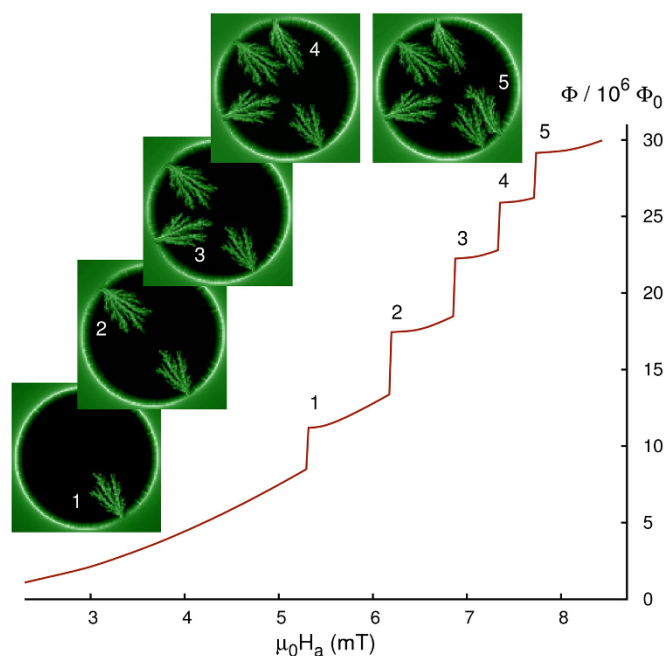


**Figure 3 | Magnetic flux in the sample versus field.** The graph displays the total magnetic flux,  $\Phi$ , inside the sample as the applied field is increased in the simulations. The avalanche events are seen as a sequence of vertical steps in the curve. The amount of flux is measured in millions of flux quanta  $\Phi_0 = h/2e$ . The five images show the flux distribution right after each event has occurred in the sequence (1)–(5).

the simulations. Shown in Fig. 4a and b are the maximum values  $E_{\max}$  and  $T_{\max}$  in the disk area recorded as the magnetic field is increasing.

At small  $H_a$  the  $E$ -field is fairly small, typically in the range of 0.1–1 V/m. Due to the disorder introduced in the model, the electric field fluctuates and the location of  $E_{\max}$  is not fixed, though it is always found near the edge. The overall trend is that  $E_{\max}$  steadily increases with  $H_a$ , a behaviour which is in agreement with the Bean model where  $E \propto \dot{H}_a H_a$  at small magnetic fields<sup>25</sup>. Yet, our  $E_{\max}$  is considerably larger than the maximum value in a uniform disk, which is  $E = \mu_0 \dot{H}_a R/2 = 0.01$  V/m in the Bean model at full flux penetration<sup>35</sup>. The fairly strong fluctuations seen in the  $E$ -field up to  $\mu_0 H_a = 5.3$  mT suggest that the flux penetration proceeds in small bursts. Such micro-avalanches, which locally enhance the  $E$ -field, then become potential nucleation sites for the largescale events. Indeed, previous MOI studies have reported observations fully consistent with this picture<sup>36,37</sup>.

At  $\mu_0 H_a = 5.3$  mT the first big event strikes, leading to a spike in  $E_{\max}$  peaking at nearly 10 kV/m. Immediately after, the  $E$ -field drops by five orders of magnitude. Then, over a substantial ramping interval the  $E_{\max}$  stays far below the value it had before the event. This means that micro-avalanches are strongly suppressed for some period. As  $H_a$  continues increasing the maximum  $E$ -field gradually returns to the pre-event level, and the next breakdown occurs 1 mT after the previous one. The graph (Fig. 4a) shows that the same characteristic behavior is found before and after each big event.

The maximum temperature over the disk area (Fig. 4b) is initially equal to the substrate temperature, and the superconductor is thermally uniform. As the magnetic field increases, precursors of a big event begin to appear as noise also in  $T_{\max}$ . From  $\mu_0 H_a \approx 4$  mT the fluctuations increase in amplitude, and at 5.3 mT the temperature shoots up to  $T_{\max} = 1.3T_c$ . Thus, during the breakdown superconductivity is lost in part of the sample. As for the electric field, right after the event the fluctuations in  $T_{\max}$  are suppressed, before they gradually reappear as the ramping of  $H_a$  continues. Similar to  $E_{\max}$ ,

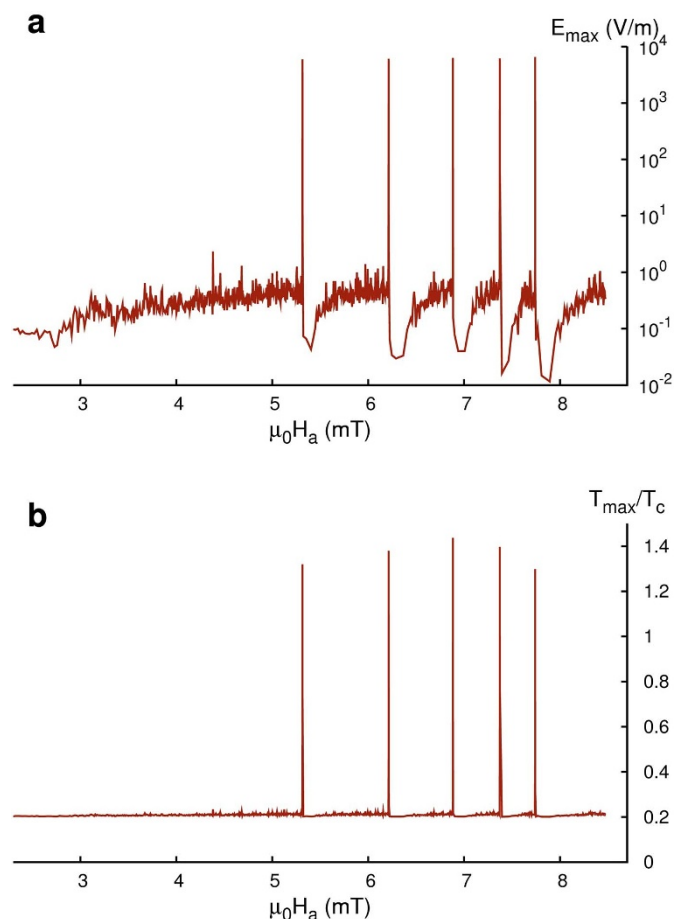


**Figure 4 | Maximum electric field and temperature.** (a) Maximum local electric field during the magnetic field ramp. The  $E$ -field is shown in a logarithmic scale. (b) Maximum local temperature in the disk normalized to the critical temperature  $T_c$  of the superconductor. The base line represents the temperature of the substrate,  $T_0 = 0.2T_c$ , and the distinct spikes correspond to the five events shown in Fig. 3.

the amplitude of the fluctuations in  $T_{\max}$  prior to all the major events is nearly the same.

**Time evolution.** Consider now the detailed dynamics of one breakdown, and we choose to zoom in on the event taking place at  $\mu_0 H_a = 5.3$  mT. Shown in Fig. 5 rows (a)–(d) are five instantaneous distributions of the magnetic flux density  $B_z$ , the stream line pattern of the flow of sheet current  $J$ , the temperature  $T$ , and the electric field  $E$ , respectively. The snapshots show the states at  $t = 1, 5, 22, 52$  and 86 ns after nucleation of the instability. The time evolution of  $B_z$  and  $T$  can be seen in Supplementary Movie 2.

The invading flux, row (a), develops from being at  $t = 1$  ns only a small protrusion on top of the critical state, to become a large dendritic structure after 86 ns. Already at  $t = 5$  ns a branching process has started, and at  $t = 22$  ns the second generation branches are clearly visible. Between  $t = 52$  and 86 ns the structure develops less fast. The final flux distribution looks quite similar to those reported from many MOI experiments<sup>2–19</sup>. Interestingly, it is essentially impossible to tell from the distribution at  $t = 22$  ns whether it is the final or an intermediate state of the flux avalanche. Indeed, considerable self-similarity in the evolving flux pattern has been reported also from ultra-fast MOI experiments<sup>5–7</sup>.

In the image at  $t = 52$  ns, the location marked (A) shows an example of one type of branching, namely where a side branch starts growing from an already existing main branch. Another type of branching can be seen at location (B), where the tip of a growing



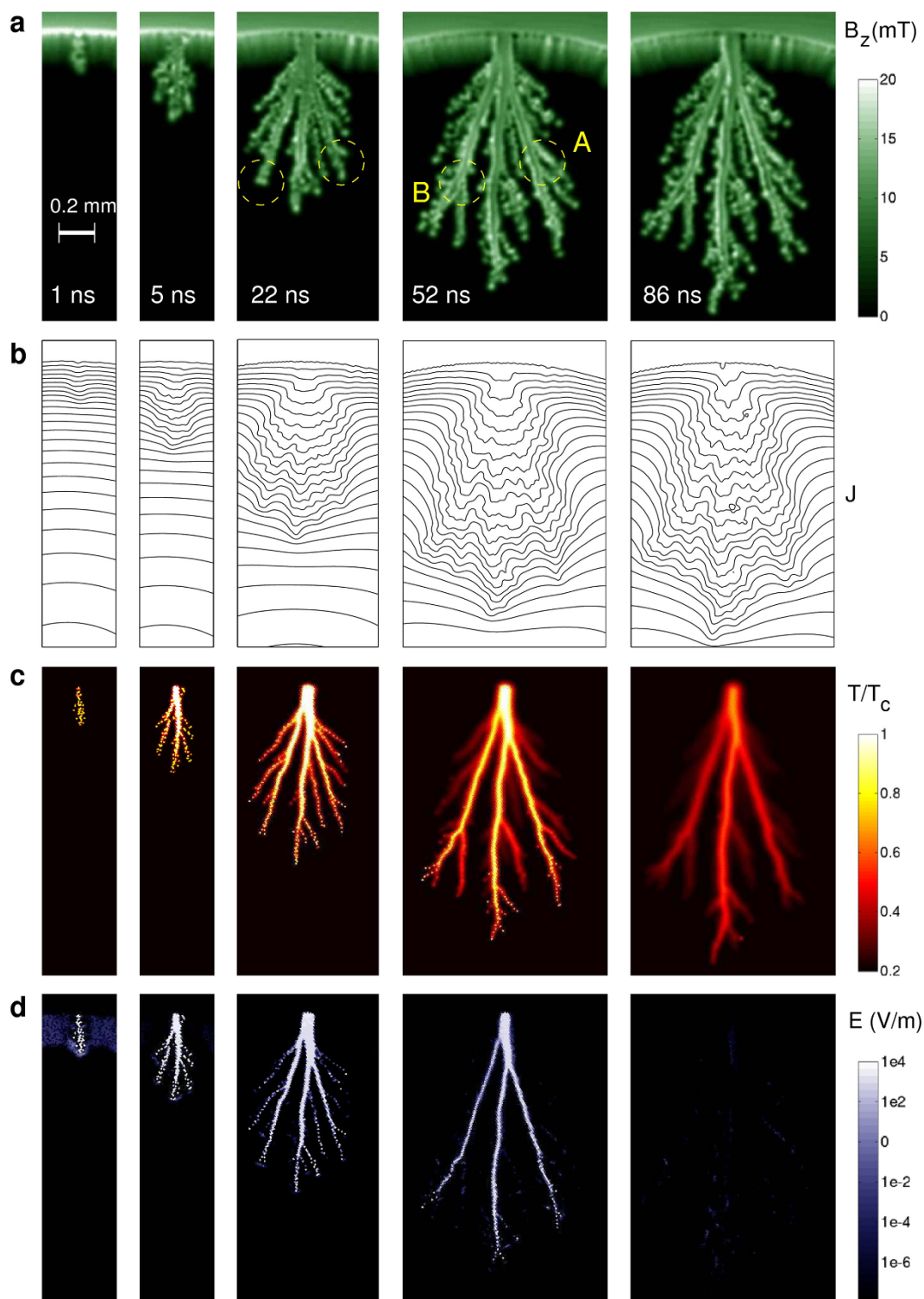


**Figure 5 | Evolution of a breakdown event.** (a) Distributions of the magnetic flux density  $B_z$ , (b) the induced sheet current  $J$ , (c) the temperature  $T$ , and (d) the electrical field  $E$ , at times  $t = 1, 5, 22, 52$  and  $86$  ns after nucleation of the thermo-electromagnetic instability.

branch suddenly splits almost symmetrically, and both new branches grow simultaneously ending up equally long. The simulations show that the latter type is the less frequent branching process. From the row of  $B_z$  images one can also see that the branches stop developing at different times. The main branches grow throughout the whole event and become the longest, not because of an extreme growth rate but because they develop over a long time span. The flux density is quite uniform along the branches, and has values that can exceed  $\mu_0 H_a$  by a

factor of two or even more. Note also that along the central part of some branches the flux density is strongly reduced. Both these characteristics reproduce features reported from previous experiments<sup>2,9,10</sup>.

Row (b) shows how the current flow pattern evolves from an initial critical-state flow, where the stream line density is constant in the flux-penetrated region, to a complex flow pattern developing as the avalanche proceeds. A front of high current density follows the expanding perimeter of the growing flux structure, leaving behind

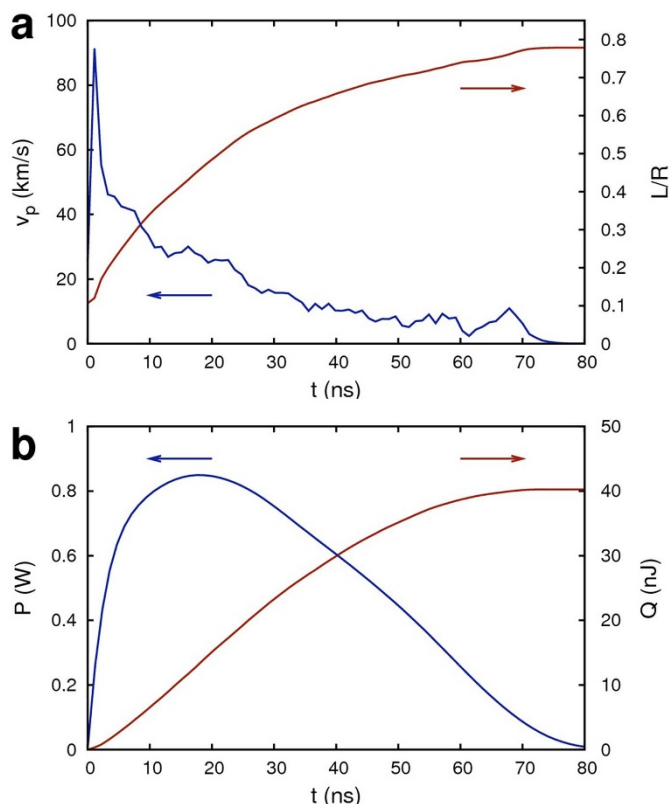


**Figure 6 | Velocity and dissipation.** (a) Length,  $L$ , of the longest branch in a flux avalanche, and its propagation velocity,  $v_p$ , as functions of time. (b) Transient behavior of the heat production rate  $P$  in the disk and the integrated heat release  $Q$ .

regions of sub-critical current density. Reduced current density inside the frozen dendritic structure has also been seen experimentally<sup>13,38</sup>. Note that in addition to the currents flowing along the branches, there is also a component of uniform current flowing through the entire dendritic structure. This transverse current acts as a driving force for the propagation of the flux avalanche.

Row (c) displays the elevated temperature  $T$ , which has the same overall dendritic signature as the flux density. Already after 1 ns a heated region extends from the edge to the flux front. In the next three panels, the branching structures develop rapidly, quite similar to the pattern of the moving flux. The avalanche stops propagating when heat removal to the substrate eventually balances the heat production. This is seen in the final panel, where the maximum temperature has already decayed to  $0.7T_c$ . Shortly after that no thermal traces are left from this dramatic event where superconductivity was lost for a very short period of time.

At all stages, the  $T$ -maps give a very good view of the dynamics, since only the moving branches are producing heat and excess heat is rapidly removed due to the good thermal contact with the substrate. Even after  $t = 22$  ns, some of the minor branches are relatively cold (dark red), indicating that here the heat generation is reduced. The maximum temperature is all the time found in the trunk of the dendritic structure, and most of the time it exceeds  $T_c$ . The tip of the branches are heated significantly, but the temperature is less than  $T_c$ .

Row (d) shows the distributions of the electric field,  $E$ , where the magnitude is displayed on a logarithmic scale. Evidently, there is a strong correlation between the regions with high  $E$ -field, and the regions of large temperature rise. One finds here  $E$ -fields up to several kV/m, which is consistent with  $\rho_0 j_c(T_0) = 6.7$  kV/m, as expected when the sample enters the Ohmic regime. This therefore suggests that the high electric fields are created while the supercurrents with

critical current density  $j_c$  for a short time flow locally with Ohmic resistivity.

**Velocity and dissipation.** From the simulations one can extract also the rate of propagation of the dendritic structures. Let  $L$  denote the distance from the sample edge to the tip of the flux branch penetrated deepest into the disk. For the event shown in Fig. 5 one obtains the curve for  $L(t)$  displayed in Fig. 6a. The  $L(0) = 0.12R$  is the overall flux penetration depth prior to the event. After  $t = 75$  ns the motion is over, ending with  $L = 0.78R$ , which gives an average velocity of 18 km/s. The plot includes also the instantaneous propagation velocity,  $v_p(t) = dL/dt$ , of the avalanche. Right after onset the speed is close to 90 km/s, and then decaying during 50 ns to values near 10 km/s, a behaviour in very good quantitative agreement with experimental results<sup>5,6</sup>. Note that the initial velocity exceeds the speed of sound, and the propagation at this stage is driven by the nonlocal electrodynamics and adiabatic heating rather than by thermal diffusion; see the Discussion section for quantitative estimates of characteristic times.

Presented in Fig. 6b is the transient behaviour of the heat dissipation rate,  $P(t) = \int_{\text{disk}} d^2r JE$ . It rises to a maximum of nearly 1 W after approximately 20 ns. The subsequent decay is essentially a consequence of the active area of the avalanche beginning to shrink. This is fully consistent with the  $E$ -field maps of Fig. 5 where the dendritic structure at  $t = 22$  ns is the largest in size and intensity. Included in the plot is also a graph of the released heat,  $Q(t) = \int_0^t dt' P(t')$ , which during the event amounts to a total of 40 nJ.

High time-resolution plots of  $T_{\text{max}}$  and  $E_{\text{max}}$  during the breakdown event are shown in Fig. 7. The transient behavior of  $T_{\text{max}}$  is similar to that of the integral dissipation rate,  $P(t)$ . The main differences are that the peak temperature occurs earlier, only 10 ns

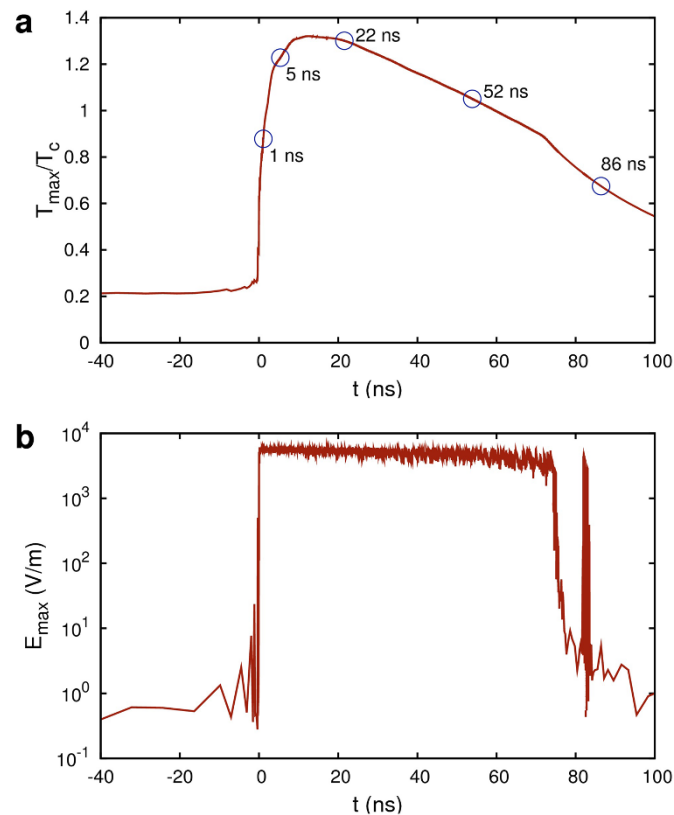


**Figure 7 | Transient temperature and electrical field.** Global maximum temperature (a) and  $E$ -field (b) in the disk as functions of time during the breakdown event. The points marked on the  $T$ -curve correspond to the five temperature distribution shown in Fig. 5. Note also that both these graphs are zooming in on the first spike in the plots of Fig. 4.



after instability onset, and that the temperature pulse decays slower, which is due to the thermal inertia of the system. Note from the graph that just prior to onset of the event, the  $T_{\max}$  increases by 1–2 K during a 2 ns period. This is consistent with our suggestion that micro-avalanches form the triggering mechanism of the breakdown. This is further supported by the behavior of the  $E_{\max}$  in the graph below. There one sees a clear signature of micro-avalanches taking place during the last couple of nanoseconds before  $E_{\max}$  abruptly jumps by four orders of magnitude. Interestingly, the  $E$ -field also reveals that a very short-lived event takes place approximately 10 ns after the main event terminated.

## Discussion

The present simulations have revealed several important time scales characterizing the nucleation and subsequent evolution of the thermo-electromagnetic breakdown in type-II superconducting films. Most notably, we find that the rise time of such events, described by how fast the electric field rises to its maximum (Fig. 7b), is extremely short: of the order of 1 ns. The total duration of an event is 75–80 ns, while the nucleation of a new branch takes less than 5 ns (Fig. 5). The physical origin of these time scales can be understood by considering a combination of several physical processes, discussed one by one below.

Firstly, the adiabatic heating time  $\tau_a$  describes the shortest possible time to increase the temperature from  $T_0$  to  $T_c$ . This characteristic time is estimated by considering Ohmic Joule heating, and solving  $c\dot{T} = \rho_0 j_c^2(T_0)$ , where  $c = c(T_c)(T/T_c)^3$  is the specific heat. Integrating this equation gives

$$\tau_a = c(T_c)T_c/4\rho_0 j_c^2(T_0), \quad (1)$$

where a small term  $\sim (T_0/T_c)^4$  is ignored. Using the material parameters given in the Methods section, the numerical value becomes  $\tau_a = 0.5$  ns, which indeed is very close to the rise time of the simulated events.

Secondly, the electromagnetic time scale  $\tau_{em}$  describes the lifetime of normal currents. For a thin disk, Brandt has found that the longest surviving mode has a decay time given by<sup>39</sup>

$$\tau_{em} = 0.18\mu_0 R d / \rho_0. \quad (2)$$

With the present parameters, this gives  $\tau_{em} = 1.9$  ns. Note that in the bulk case such a time constant cannot be defined since the flux motion is then described by a diffusion equation. In films, on the other hand, the flux penetration is accelerated by the presence of a free surface. The decay time is related to the propagation velocity of the peak in the current density, which is  $v_{em} = 0.77\rho_0/\mu_0 d = 0.14R/\tau_{em} = 140$  km/s<sup>39</sup>. This value provides the upper bound for the propagation velocity of the dendrite. Indeed, the initial dendrite tip velocity  $\sim 90$  km/s of Fig. 6 is not far from  $v_{em}$ .

Thirdly, heat removal to the substrate leads to an exponential decay of the temperature with a time constant

$$\tau_h = cd/h = 52 \text{ ns}, \quad (3)$$

where  $h$  is the coefficient of heat transfer to the substrate. This decay time is much longer than both  $\tau_a$  and  $\tau_{em}$ , fully consistent with the fact that the events actually do take place, rather than being prevented by an efficient heat sink provided by the substrate. The value of  $\tau_h$  is comparable to the total duration of the event, suggesting that the heat removal to the substrate largely determines the avalanche life-time, and thereby also decides the size of the full-grown flux dendrite.

Finally, the lateral heat transport is an ordinary diffusion process with diffusion time

$$\tau_\kappa = l^2 c / 4\kappa, \quad (4)$$

where  $l$  is the diffusion length and  $\kappa$  is the thermal conductivity. The diffusion length characteristic for the dendrite tips can be obtained

from the  $T$ -maps of Fig. 5, where the very sharp tips of the growing branches have a typical width  $l = 10 \mu\text{m}$ , which gives  $\tau_\kappa = 5.1$  ns. This is close to the characteristic time for the first branching to occur, indicating that the heat diffusion plays an important role for the way the branch width evolves.

Considering the other extreme, and letting  $\tau_\kappa$  be the total duration of an event, 75 ns, we obtain the largest relevant diffusion length,  $l = 38 \mu\text{m}$ . This is much smaller than the length of the long branches in the dendritic structure, but interestingly it is approximately half the width of the dendrite trunk at the final stage. This indicates that the trunk is gradually widened by heat diffusion during the event.

All these characteristic times are much shorter than the time scale of the background flux penetration, which is on the order of milliseconds. Therefore, our results on the evolution of the instability are essentially independent of the ramp rate of the applied magnetic field. This robustness is consistent with numerous MOI experiments performed by some of the present authors.

Comparison of the characteristic times shows that the propagation of flux avalanches in superconducting films placed in a transverse applied magnetic field is at the initial stage driven by nonlocal electro-dynamics and adiabatic heating rather than by thermal diffusion. The thermal aspects of the present phenomenon have similarities to a moving hot spot generated by a laser beam swept across a surface at supersonic speed. The temperature profile is then determined by adiabatic heating from the fast moving source. Very fast flux propagation due to adiabatic heating by the electromagnetic field outside a superconducting film was first pointed out in Ref. 28. Since  $\tau_a \ll \tau_\kappa$ , in the initial (supersonic) stage of flux propagation the thermal diffusion plays only a minor role. During later (subsonic) stages, thermal diffusion in the avalanche propagation direction will only slightly smear the temperature distribution formed by the local adiabatic heating. In the direction perpendicular to the avalanche, however, the thermal diffusion is indeed important as it leads to branching and determines the width of the branches. We have confirmed this by performing additional simulations for different values of  $\kappa$ .

In conclusion, by using a numerical method we have simulated the coupled dynamics of magnetic flux, electrical field and local temperature in superconducting films placed in a time-dependent transverse applied magnetic field. The calculations were performed for a disk-shaped thin sample with a set of parameters representative for MgB<sub>2</sub>, a material where breakdown events are frequently observed, but so far no experiments could resolve the ultra-fast dynamics.

The temporal characteristics of the events are extreme, as the flux front propagates with the speed of 100 km/s and the whole event is over in less than 100 ns. We have found that the dendritic features first appear approximately 5 ns after the instability onset, when the root splits into branches that propagate into the flux-free interior of the sample. From that moment on, the morphology of the flux pattern is essentially self-similar, and maintained by side branches growing from the main branches as the structure expands. Occasionally, the branch tips will bifurcate symmetrically. The maximum temperature is found at the main trunk of the dendritic structure, where it reaches  $(1.2 - 1.4)T_c$ , obviously fatal for the local superconducting properties, and extremely harmful for a device based on such a superconducting film. In the same region, also the electric field is maximum, with values close to the theoretical maximum,  $\rho_0 j_c(T_0) = 6.7$  kV/m, reached almost immediately,  $t \lesssim 1$  ns, after nucleation of the event. The maximum dissipation rate is approximately 1 W.

Prior to an event we find large fluctuations in both temperature and electric field. They are interpreted as traces of micro-avalanches, a phenomenon that so far has attracted little attention. We argue that these fluctuations are of prime importance, since they may well be the stochastic triggering mechanism causing the large-scale breakdown.

Our results are in good agreement with the very few experimental works reporting on the time-resolved intermittent behavior in





superconducting films. Since adequate experimental tools are almost non-existent, our simulations method can be essential for the further exploration of the nucleation and evolution of these dramatic irreproducible and unpredictable lightning-like events.

## Methods

**Basic equations and numerical approach.** The sample is a disk with radius  $R$  and thickness  $d \ll R$ , placed in an applied magnetic field  $H_a$  directed transverse to the disk plane, see Fig. 1. We treat the magnetic flux density  $B_z$  as a continuum variable satisfying the Maxwell equations, and assume a vanishing first critical field,  $H_{c1} = 0$ , implying that  $\mathbf{B} = \mu_0 \mathbf{H}$  also inside the superconductor<sup>35</sup>.

The material characteristics is modelled by the commonly used phenomenological non-retarded  $E - J$  relation<sup>25</sup>,

$$\mathbf{E} = \frac{\rho \mathbf{J}}{d}, \quad \rho \equiv \begin{cases} \rho_0 & J > J_c(T), \\ \rho_0 (J/J_c)^{n-1} & \text{otherwise.} \end{cases} \quad (5)$$

Here  $\mathbf{E}$  is the electric field,  $\mathbf{J}$  is the sheet current with  $|\mathbf{J}| = J$ ,  $\rho_0$  is the normal state resistivity,  $J_c$  is the critical sheet current, and  $n$  is the creep exponent. For  $T \leq T_c$  the temperature dependencies of  $J_c$  and  $n$  are specified as

$$J_c = J_{c0} (1 - T/T_c), \quad n = n_1 (T_c/T) - n_0. \quad (6)$$

This model describes thermally activated hopping of vortices, the effective velocity being  $\propto e^{-U_0/kT}$  with  $U = U_0 \ln(J_c/J)$ . The model captures main features of nonlinear vortex dynamics and turns out to be very successful in understanding results of numerous experiments, see, e.g., Ref. 41 for a review.

The sheet current density is expressed through the local magnetization,  $g(x, y)$ , as<sup>25</sup>

$$\partial g / \partial y = J_x, \quad \partial g / \partial x = -J_y, \quad (7)$$

which ensures conservation of current,  $\nabla \cdot \mathbf{J} = 0$ . As described in Ref. 32, the time derivative of  $g$  can be obtained by inversion of the Biot-Savart law, which is expressed by

$$\dot{g} = \mathcal{F}^{-1} [(2/k) \mathcal{F} (\dot{B}_z / \mu_0 - \dot{H}_a)]. \quad (8)$$

Here  $\mathcal{F}$  and  $\mathcal{F}^{-1}$  denote, respectively, the direct and inverse Fourier transforms with respect to spatial coordinates, and  $k = |\mathbf{k}|$  where  $\mathbf{k}$  is the in-plane wave vector. In Eq. (8) the three-dimensional Maxwell equations have been transformed to a non-local two-dimensional equation. The non-locality is a consequence of the in-plane magnetic fields present at both surfaces of the film. The non-local electrostatics of a thin film in the transverse geometry is the reason for fast propagation of flux dendrites with characteristic speeds exceeding microscopic electron and phonon scales such as the sound velocity.

The time evolution of the temperature is modelled by the heat propagation equation,

$$c \dot{T} = \nabla \cdot (\kappa \nabla T) - (h/d)(T - T_0) + \mathbf{J} \cdot \mathbf{E} / d. \quad (9)$$

Here  $T_0$  is the substrate temperature assumed to be constant,  $c$  is the specific heat. In the simulations we assume that  $c$ ,  $h$  and  $\kappa$  are all proportional to  $T^3$ . These dependencies are compatible with available experimental results<sup>30,40</sup>. Since the characteristic phonon times are much shorter than the typical time scales for the development of the avalanche we neglect the delay in the thermal response, i. e., assume that both  $\kappa$  and  $h$  do not explicitly depend on time.

Equation (9) assumes that both electrons and phonons are characterized by quasi-equilibrium distributions with the same temperature. This is expected when the microscopic relaxation times corresponding to electron-electron, electron-phonon and phonon-phonon scattering are much shorter than the typical evolution times of the present thermo-magnetic propagation process. In addition, the mean free paths of the electrons and phonons should be much less than typical dimensions of the dendritic patterns. Estimates show that these requirements are met in the present situation.

The evolution of  $g$  and  $T$  is computed by discrete time integration of Eqs. (8) and (9). The plane  $z = 0$  is arranged as a square superlattice where each cell has size  $2a \times 2a$ , with  $a > R$ . The superconducting disk is placed centrally inside the cell and surrounded by vacuum. Then, within the superconductor,  $B_z$  is found from Faraday's law,  $\dot{B}_z = -(\nabla \times \mathbf{E})_z$ , combined with the material law, Eq. (5). In the surrounding vacuum,  $\dot{B}_z$  is obtained by a self-consistent iterative scheme which ensures  $\dot{g} = 0$  there. Eq. (8) was integrated forward in time with the fourth order Runge-Kutta method, while the Eq. (9) was integrated by a forward/backward time average to ensure stable results. A detailed description of the computational scheme is found in Ref. 32.

The simulations were run on a square of half-width  $a = 1.2R$ , and discretized on a  $512 \times 512$  equidistant grid. A weak quenched disorder was introduced by randomly increasing or decreasing  $J_{c0}$  of each grid point by 5%. In addition, fluctuations were introduced by randomly alternating between the left and the right derivatives when computing  $\nabla \times \mathbf{E}$  in the Faraday law.

**Material parameters.** The following parameters, typical for films of  $\text{MgB}_2$ , were used in the calculations<sup>30,32,40</sup>:  $T_c = 39$  K,  $\rho_0 = 7 \mu\Omega \cdot \text{cm}$ , and a critical current density  $j_{c0} =$

$J_{c0}/d = 1.2 \cdot 10^{11}$  A/m<sup>2</sup>. The thermal parameters were chosen as  $\kappa = 0.17 (T/T_c)^3$  kW/Km,  $c = 35 (T/T_c)^3$  kJ/Km<sup>3</sup>, and  $h = 200 (T/T_c)^3$  kW/Km<sup>2</sup>. We used  $n_1 = 20$ ,  $n_0 = 10$ , and restricted  $n(T)$  to  $n \leq 59$  at low temperatures. The disk dimensions were  $R = 2$  mm and  $d = 0.3 \mu\text{m}$ . Substrate temperature was  $T_0 = 0.2T_c$  and the applied magnetic field was ramped at the constant rate,  $\dot{H}_a = 2.4 \cdot 10^{-6} j_{c0} \rho_0 / R \mu_0$ .

- Altshuler, E. & Johansen, T. H. *Colloquium: Experiments in vortex avalanches. Rev. Mod. Phys.* **76**, 471 (2004).
- Durán, C. A., Gammel, P. L., Miller, R. E. & Bishop, D. J. Observation of magnetic field penetration via dendritic growth in superconducting niobium films. *Phys. Rev. B* **52**, 75 (1995).
- Welling, M. S., Westerwaal, R. J., Lohstroh, W. & Wijngaarden, R. J. Huge compact flux avalanches in superconducting Nb thin films. *Physica C* **411**, 11 (2004).
- P. Brüll, D., Kirchgässner, Leiderer, P., Berberich, P. & Kinder, H. Magnetic field-induced damage in a superconducting  $\text{YBa}_2\text{Cu}_3\text{O}_{7-\delta}$ . *Ann. Phys. (Leipzig)* **1**, 243 (1992).
- Leiderer, P., Boneberg, J., Brüll, P., Bujok, V. & Herminghaus, S. Nucleation and growth of a flux instability in superconducting  $\text{YBa}_2\text{Cu}_3\text{O}_{7-x}$  films. *Phys. Rev. Lett.* **71**, 2646–2649 (1993).
- Bolz, U., Biehler, B., Schmidt, D., Runge, B. & Leiderer, P. Dynamics of the dendritic flux instability in  $\text{YBa}_2\text{Cu}_3\text{O}_{7-\delta}$ . *Europhys. Lett.* **64**, 517 (2003).
- Bolz, U. *et al.* Dendritic and homogenous regimes of flux penetration into YBCO films. *Physica C* **388–399** (2003).
- Vlasko-Vlasov, V., Welp, U., Metlushko, V. & Crabtree, G. W. Flux avalanches in superconducting films with periodic array of holes. *Physica C* **341**, 1281 (2000).
- Johansen, T. H. *et al.* Dendritic magnetic instability in superconducting  $\text{MgB}_2$  films. *Europhys. Lett.* **59**, 599 (2002).
- Barkov, F. L. *et al.* Local threshold field for dendritic instability in superconducting  $\text{MgB}_2$  films. *Phys. Rev. B* **67**, 064513 (2003).
- Albrecht, J. *et al.* Bending of magnetic avalanches in  $\text{MgB}_2$  thin films. *Appl. Phys. Lett.* **87**, 182501 (2005).
- E.-M. Choi *et al.* Dendritic magnetic avalanches in carbon-free  $\text{MgB}_2$  thin films with and without a deposited Au layer. *Appl. Phys. Lett.* **87**, 152501 (2005).
- Olsen, A. A. F. *et al.* Flux dendrites of opposite polarity in superconducting  $\text{mgB}_2$  rings observed with magneto-optical imaging. *Phys. Rev. B* **74**, 064506 (2006).
- Ghigo, G. *et al.* Evidence of rf-driven dendritic vortex avalanches in  $\text{MgB}_2$  microwave resonators. *J. Appl. Phys.* **102**, 113901 (2007).
- Treiber, S., Stahl, C., Schütz, G. & Albrecht, J. Stability of the current-carrying state in nonhomogeneous  $\text{MgB}_2$  films. *Phys. Rev. B* **84**, 094533 (2011).
- Rudnev, I. A., Antonenko, S. V., Shantsev, D. V., Johansen, T. H. & Primenko, A. E. Dendritic flux avalanches in superconducting  $\text{Nb}_3\text{Sn}$  films. *Cryogenics* **43** (2003).
- Wimbush, S. C., Holzapfel, B. & Ch. Jooss. Observation of dendritic flux instabilities in  $\text{YNi}_2\text{B}_2\text{C}$  thin films. *J. App. Phys.* **96**, 3589 (2004).
- Rudnev, I. A., Shantsev, D. V., Johansen, T. H. & Primenko, A. E. Avalanche-driven fractal flux distributions in  $\text{NbN}$  superconducting films. *Appl. Phys. Lett.* **87**, 04202 (2005).
- Yurchenko, V. V. *et al.* Reentrant stability of superconducting films and the vanishing of dendritic flux instability. *Phys. Rev. B* **76**, 092504 (2007).
- Motta, M. *et al.* Anomalous flux avalanche morphology in a a-MoGe superconducting film with a square antidot lattice - experiment and simulation (2011). 1109.2532v1.
- Mints, R. G. & Rakhmanov, A. L. Critical state stability in type-II superconductors and superconducting-normal-metal composites. *Rev. Mod. Phys.* **53**, 551 (1981).
- Colauto, F. *et al.* Suppression of flux avalanches in superconducting films by electromagnetic breaking. *Appl. Phys. Lett.* **96**, 092512 (2010).
- Lee, J. *et al.* Saw-tooth pattern from flux jumps observed by high resolution M-H curves in  $\text{MgB}_2$  thin films. *J. Appl. Phys.* **108**, 033909 (2010).
- Goa, P. E., Hauglin, H., Olsen, A. A. F., Baziljevich, M. & Johansen, T. H. Magneto-optical imaging setup for single vortex observation. *Rev. Sci. Instrum.* **74**, 141 (2003).
- Brandt, E. H. Electric field in superconductors with rectangular cross section. *Phys. Rev. B* **52**, 15442 (1995).
- Mints, R. G. & Brandt, E. H. Flux jumping in thin films. *Phys. Rev. B* **54**, 12421 (1996).
- Rakhmanov, A. L., Shantsev, D. V., Galperin, Y. M. & Johansen, T. H. Finger pattern produced by thermomagnetic instability in superconductors. *Phys. Rev. B* **70**, 224502 (2004).
- Aranson, I. S. *et al.* Dendritic flux avalanches and nonlocal electrostatics in thin superconducting films. *Phys. Rev. Lett.* **94**, 037002 (2005).
- Denisov, D. V., Rakhmanov, A. L., Shantsev, D. V., Galperin, Y. M. & Johansen, T. H. Dendritic and uniform flux jumps in superconducting films. *Phys. Rev. B* **73**, 014512 (2006).
- Denisov, D. V. *et al.* Onset of dendritic flux avalanches in superconducting films. *Phys. Rev. Lett.* **97**, 077002 (2006).
- Albrecht, J. *et al.* Dramatic role of critical current anisotropy on flux avalanches in  $\text{MgB}_2$  films. *Phys. Rev. Lett.* **98**, 117001 (2007).
- Vestgård, J. I., Shantsev, D. V., Galperin, Y. M. & Johansen, T. H. Dynamics and morphology of dendritic flux avalanches in superconducting films. *Phys. Rev. B* **84**, 054537 (2011).



33. Mikheenko, P. N. & Kuzovlev, Y. E. Inducance measurements of HTSC films with high critical currents. *Physica C* **229** (1993).
34. Clem, J. R. & Sanchez, A. Hysteric ac losses and susceptibility of thin superconducting disks. *Phys. Rev. B* **50**, 9355 (1994).
35. Brandt, E. H. Susceptibility of superconductor disks and rings with and without flux creep. *Phys. Rev. B* **55**, 14513 (1997).
36. Altshuler, E. *et al.* Vortex avalanches with robust statistics observed in superconducting niobium. *Phys. Rev. B* **70**, 140505 (2004).
37. Shantsev, D. V., Bobyl, A. V., Galperin, Y. M., Johansen, T. H. & Lee, S. I. Size of flux jumps in superconducting films. *Phys. Rev. B* **72**, 024541 (2005).
38. Laviano, F. *et al.* Thermo-magnetic instability as limiting mechanism for electrical current density in MgB<sub>2</sub> thin films. In Johansen, T. H. & Shantsev, D. V. (eds.) *Magneto-Optical Imaging*, 237 (Kluwer Academic, 2004).
39. Brandt, E. H. Thin superconductors in a perpendicular magnetic ac field. ii. circular disk. *Phys. Rev. B* **50**, 4034–4050 (1994).
40. Schneider, M. *et al.* Heat and charge transport properties of MgB<sub>2</sub>. *Physica C* **363**, 6 (2001).
41. Blatter, G. *et al.* Vortices in high-temperature superconductors. *Rev. Mod. Phys.* **66**, 1125 (1994).

## Acknowledgments

We are thankful to Valerii Vinokur for valuable discussions. The financial support of the Research Council of Norway is acknowledged. YG is thankful to Max Planck Institute for Physics of Complex Systems, Dresden, Germany for hospitality.

## Author contributions

J.I.V. conducted the simulation and wrote the paper draft. All authors contributed to the planning, discussions, and writing of the manuscript. The magneto-optical image was taken by T.H.J. and Å.A.F.Olsen.

## Additional information

**Supplementary information** accompanies this paper at <http://www.nature.com/scientificreports>

**Competing financial interests:** The authors declare no competing financial interests.

**License:** This work is licensed under a Creative Commons Attribution-NonCommercial-NoDerivs 3.0 Unported License. To view a copy of this license, visit <http://creativecommons.org/licenses/by-nc-nd/3.0/>

**How to cite this article:** Vestgård, J.I., Shantsev, D.V., Galperin, Y.M. & Johansen, T.H. Lightning in superconductors. *Sci. Rep.* **2**, 886; DOI:10.1038/srep00886 (2012).